Measurement Science
and Technology

100 year anniversary
Measurement Science and Technology

PURPOSE-LED
PUBLISHING™

PAPER • **OPEN ACCESS**

Comparison of camera calibration methods for particle tracking velocimetry

To cite this article: R Barta *et al* 2025 *Meas. Sci. Technol.* **36** 055301

OPEN ACCESS
IOP Publishing
Measurement Science and Technology
Meas. Sci. Technol. **36** (2025) 055301 (17pp)
https://doi.org/10.1088/1361-6501/adc6a2

Comparison of camera calibration methods for particle tracking velocimetry

R Barta[1,*], **A Liberzon**[2] **and R Shnapp**[3]

[1] Institute of Aerodynamics and Flow Technology, German Aerospace Center (DLR), Bunsenstraβe 10, Göttingen 37073, Germany
[2] Turbulence Structure Laboratory, School of Mechanical Engineering, Tel Aviv University, Tel Aviv, Israel
[3] Department of Mechanical Engineering, Ben Gurion University, Tel Aviv, Israel

E-mail: robin.barta@dlr.de

Received 28 October 2024, revised 25 February 2025
Accepted for publication 28 March 2025
Published 15 April 2025

Abstract

Camera calibration is a key component of three-dimensional particle tracking velocimetry (PTV) experiments, and its proper implementation is key to the success of the method. In this paper, we review and compare four different camera calibration models used in PTV experiments without volumetric refinement. One of the calibration models is new and provides an analytical inversion of the Soloff polynomial. The other three calibration models are taken from three established open source PTV frameworks: OpenPTV, MyPTV and proPTV. In particular, we present a general formulation of calibration models that allows their rigorous comparison and evaluation with respect to their 3D-to-2D projection errors and 2D-to-3D reconstruction errors. We compare the models and the calibration errors in three different tasks, including extrapolation and interpolation of marker points, using a realistic calibration of an experimental camera setup. In the end, we conclude with the pros and cons of each method in order to be able to choose the most suitable one for individual needs.

Keywords: experimental methods, fluid mechanics, camera calibration, particle tracking velocimetry, open-source

1. Introduction

Particle tracking velocimetry (PTV) is the name of a method in experimental fluid mechanics that uses stereo photography to measure fluid velocity fields in the Lagrangian view by tracking the moment of individual tracer particles. A central aspect of this method is the calibration of the camera setup, which involves finding a way to transform a 3D physical world coordinate system into one or more 2D camera coordinate systems and vice versa [1]. Calibration is crucial in the context of PTV as it allows us to accurately determine correspondences between the triangulated 3D position and the 2D centroid position of the imaged tracer particles [2–4]. In fact, camera calibration is used in numerous other measurement methods, both in experimental fluid mechanics, e.g. in tomographic particle image velocimetry [5], but also in other fields, such as aerial remote sensing [6], and 3D shape measurement [7]. As with any scientific measurement system, accuracy and error quantification are the key to the successful implementation of PTV, and, since positioning uncertainties are derived from calibration errors, it is necessary to achieve high-quality camera calibration always. In particular, minimizing calibration errors is essential for distinguishing close or overlapping particle intensity distributions, and thus reducing

---

[*] Author to whom any correspondence should be addressed.

errors in the reconstruction of 3D particle positions [8]. In this work, we review and compare four different methods for camera calibration in the context of PTV experiments.

Camera calibration generally comprises two main components: (1) a calibration model with a transformation function from the 3D physical world coordinates into 2D image coordinates of a camera, and (2) an optimization routine to determine the model parameters. There are various types of calibration models that can be broadly divided into two categories. Models of the first category rely on physical optics and always try to model the physical camera device, e.g. the Tsai camera model (also known as the pinhole model) with various corrections for aberration of the image [9–14]. These models aim to accurately model various optical effects, such as multimedia light refraction, however, they are often complex to set up and optimize due to their demand on an already accurate initial guesses of model parameter like the focal length, magnifications, and camera positions. The second category relies on the purely mathematical fitting of the optical correspondence from 2D to 3D coordinates via non-linear functions such as polynomials in the case of the Soloff method [15, 16]. Methods in this category tend to be more straightforward to apply because they only require a mapping of 3D physical world coordinates into 2D camera coordinates, and there are no extrinsic or intrinsic camera parameters or corrections due to refraction or lens distortion that need to be taken into account. However, such camera calibration models come with the drawback of being analytically non-invertible, meaning that 3D positions cannot be directly estimated from 2D camera coordinates, which is an important aspect of every PTV algorithm. This limitation can be addressed using numerical techniques, such as the iterative triangulation method discussed in [17]. Another drawback is that, when using purely mathematical camera models, information about the camera's physical parameters, such as the position of the camera in the 3D world, is lost.

In section 2 we introduce in detail four camera models taken from the two categories. As for model optimization, this operation is usually achieved by capturing images of an object with known dimensions, called the calibration target, and finding the calibration model parameters that minimize the discrepancy between the view of the calibration target as captured by the camera and the projection of the calibration target on the images using the 3D model (this is defined in equation (3), below). The root mean square (RMS) of the discrepancy between the image and the projection of the calibration target is called the calibration error, and this is the quantity that is usually minimized, often through optimization routines such as the least squares method [18]. Typical calibration targets are checkerboard plates [19], calibration dumbbells [20, 21], and multi-plane calibration bodies [12] or calibration plates [22, 23] with marker points imprinted on them. An optional subsequent part of model optimization is a step, often called volumetric calibration [24–26], which uses experimental results to further minimize the calibration error. However, in this paper, we will not focus on this topic, since our main comparison is to quantify the calibration errors of the calibration models themselves, using an imperfect and realistic initial calibration of a complex optical experimental setup. All in all, any calibration model with a mathematically sound 2D to 3D mapping and back from 3D to 2D can be used for PTV, but each one has its own advantages and disadvantages. The realization of this fact is the starting point of this work and our primary goal is to compare the different camera calibration models of three established open-source PTV frameworks: OpenPTV [11], MyPTV [27], and proPTV [17] in terms of applicability and precision. To achieve that, we focus on analyzing the spatial distribution of their calibration errors [28, 29], and their ability to extrapolate and interpolate around calibration markers. In addition, this study initiates a collaborative project aimed at making these open-source PTV frameworks compatible for future use, to eliminate the drawbacks of each camera calibration model by its own. One of the main results of this project is a new camera calibration model, called the inverse Soloff model, which consists of an invertible polynomial camera calibration method (section 2).

The paper is organized as follows. Section 2 introduces the fundamental definition of a camera calibration model and reviews four specific models in detail. Section 3 describes the experimental setup and the calibration procedure used for the model comparison. In section 4, we compare the calibration errors of the different calibration models using the experimental test case. Finally, in section 5 a conclusion is drawn.

2. Camera calibration models

In what follows, we begin by introducing the general notion of a camera calibration model and the ways in which it could be evaluated. Following that, we introduce four specific models that will be compared later in this work: the multimedia Tsai model [11], the polynomial Tsai model [27], the Soloff polynomial model [17] and the inverse Soloff polynomial model that is first reported in this work. In practice, each model was operated using a different open-source PTV software: OpenPTV [11], MyPTV [27], proPTV [17], and again MyPTV, respectively, for each model. All methods rely on the same definition of the coordinate system as provided in figure 2.

2.1. General formulation of a camera calibration model

At a fundamental level, any camera calibration model can be viewed as a transformation between the 2D camera coordinates x_i, y_i and the 3D physical world coordinates X, Y, Z and backward. The index i in the camera coordinate system represents a specific camera. Thus, a 3D to 2D transformation, the so-called forward transformation, is denoted as

$$\begin{bmatrix} x_i \\ y_i \end{bmatrix} = \mathcal{T}_M \left(X, Y, Z, t_i^1, \ldots, t_i^{N_M} \right) , \tag{1}$$

where $\mathcal{T}_M$ is the transformation function of the calibration model M and contains N_M parameters: $t_i^1, \ldots, t_i^{N_M}$. The inverse transformation, from 2D back to 3D coordinates, is denoted as

$$\begin{bmatrix} X \\ Y \\ Z \end{bmatrix} = \mathcal{T}_M^{-1}\left(x_1, y_1, t_1^1, \ldots, t_1^{N_M}, \ldots, x_{N_c}, y_{N_c}, t_{N_c}^1, \ldots, t_{N_c}^{N_M}\right), \tag{2}$$

where N_c is the number of cameras in the experimental system. Transformation $\mathcal{T}_M^{-1}$ requires $N_c \geqslant 2$, as at least two views are needed to triangulate the position of an object in a 3D space. From a practical point of view, N_c is usually taken to be more than 2, since redundancy helps to resolve uncertainties due to optical occlusions in particle-dense experiments and increases the accuracy of the positioning. In this work, we use $N_c = 4$ cameras. Optimizing the parameters of a given calibration model is usually done using images of a calibration target (e.g. figure 3) which is shifted by known distances at multiple positions throughout the measurement volume. The target has numerous points imprinted on it at known 3D distances, so the image of the target is used to generate a list that maps the known 3D marker positions to their estimated centroid positions on the camera images. Let us denote the 3D position of the marker j as $\vec{X}_j$ and its 2D position as $\vec{x}_j$. The discrepancy between the 2D marker position on camera i and the reprojection of the 3D marker position on the same camera by a given calibration model is then denoted by the 2D calibration error:

$$\vec{\delta}_{M,i}^{2D}\left(\vec{X}_j\right) = \mathcal{T}_M\left(\vec{X}_j, t_i^1, \ldots, t_i^{N_M}\right) - \vec{x}_j. \tag{3}$$

Optimizing the parameters of a camera calibration model is performed by searching for the set of N_M parameters that minimizes the sum $\sum_j ||\vec{\delta}_{M,i}^{2D}(\vec{x}_j)||^2$ over all calibration markers. In addition to that, the quality of a calibrated system of cameras can be evaluated by considering the discrepancies in 3D world coordinates, defined as the 3D calibration error:

$$\vec{\delta}_M^{3D}\left(\vec{X}_j\right) = \mathcal{T}_M^{-1}\left(\vec{x}_{j,1}, t_1^1, \ldots, t_1^{N_M}, \ldots, \vec{x}_{j,N_c}, t_{N_c}^1, \ldots, t_{N_c}^{N_M}\right) - \vec{X}_j. \tag{4}$$

In particular, the significant difference between $\vec{\delta}_{M,i}^{2D}$ and $\vec{\delta}_M^{3D}$ is that the former is defined per camera while the latter pertains to the reconstruction capabilities of a system comprising several cameras, and both quantities provide insightful information of the calibration errors of a given calibration model. Note that the 3D calibration error should always be displayed with respect to the smallest length scale in the system, which is the Kolmogorov length η in turbulent flows.

2.2. Multimedia Tsai model

The multi-media calibration method used in OpenPTV [11] is explained in full detail in the original work of Maas *et al* [3]. The model relies on the so-called pinhole camera optics and includes rigorous corrections of various non-linear optical phenomena such as barrel or pillow lens distortions. Furthermore, when measuring through multiple media with varying index of refraction (such as air, glass, water, which is common in PTV experiments), light refraction causes objects to appear at positions different from their actual locations, and this effect must be corrected to achieve a physical representation of the optical system. The mathematical model consists of three interconnected components that work together to provide accurate mappings $\mathcal{T}_M$ and $\mathcal{T}_{\mathcal{M}}{}^{-1}$. The first component is the scaled pinhole camera model

$$\begin{bmatrix} x_i - x_h \\ y_i - y_h \\ -f \end{bmatrix} = \lambda_i \cdot \mathbf{R} \cdot \begin{bmatrix} X - X_0 \\ Y - Y_0 \\ Z - Z_0 \end{bmatrix}, \tag{5}$$

which is expressed through the collinearity condition,

$$\begin{aligned} x_i &= x_h - f\frac{r_{11}(X - X_0) + r_{21}(Y - Y_0) + r_{31}(Z - Z_0)}{r_{13}(X - X_0) + r_{23}(Y - Y_0) + r_{33}(Z - Z_0)}, \\ y_i &= y_h - f \cdot \frac{r_{12}(X - X_0) + r_{22}(Y - Y_0) + r_{32}(Z - Z_0)}{r_{13}(X - X_0) + r_{23}(Y - Y_0) + r_{33}(Z - Z_0)}. \end{aligned} \tag{6}$$

The equations above contain the first eight model parameters. The parameters X_0, Y_0, and Z_0 represent the position of the camera in 3D physical coordinates, f is the focal length of the camera, λ_i the scale factor, x_h and y_h denote the principal point of the image, and r_{ij} denote the elements of the 3D rotation matrix $\mathbf{R}$ that is described by three independent angle components $\theta_X, \theta_Y, \theta_Z$, which define the orientation of the camera. The second component is the multimedia correction, which accounts for light refraction through different media (figure 1). Note that this correction is simplified and assumes that light rays are usually incident on the air-glass interface and that the glass slab is thin compared to the other dimensions of the problem. In a more general case, the calculation would involve more complex geometry and trigonometry [30–32]. In OpenPTV, similarly to the original work [3], only a radial shift of each object point relative to the axis of projection of the camera center point O (marked by a vertical dashed line) is estimated, as demonstrated in figure 1. The multimedia correction starts by calculating the radial distance R from the camera axis for a given point with 3D coordinates X, Y, Z

$$R = \sqrt{(X - X_0)^2 + (Y - Y_0)^2}, \tag{7}$$

and the refraction angles using Snell's law:

$$n_1 \sin(\beta_1) = n_2 \sin(\beta_2) = n_3 \sin(\beta_3), \tag{8}$$

to finally calculate the actual radial distance $\hat{R}$ and the apparent radial distance R. The following equations are used with the refractive indices of air, glass, water: n_1, n_2, n_3, the thicknesses of the medium air, glass, and water: Z_1, Z_2, Z_3 and the refraction angles of air, glass, and water: β_1, β_2, β_3

$$\hat{R} = Z_1 \tan(\beta_1) + Z_2 \tan(\beta_2) + Z_3 \tan(\beta_3) \tag{9}$$

$$R = (Z_1 + Z_2 + Z_3)\tan(\beta_1). \tag{10}$$

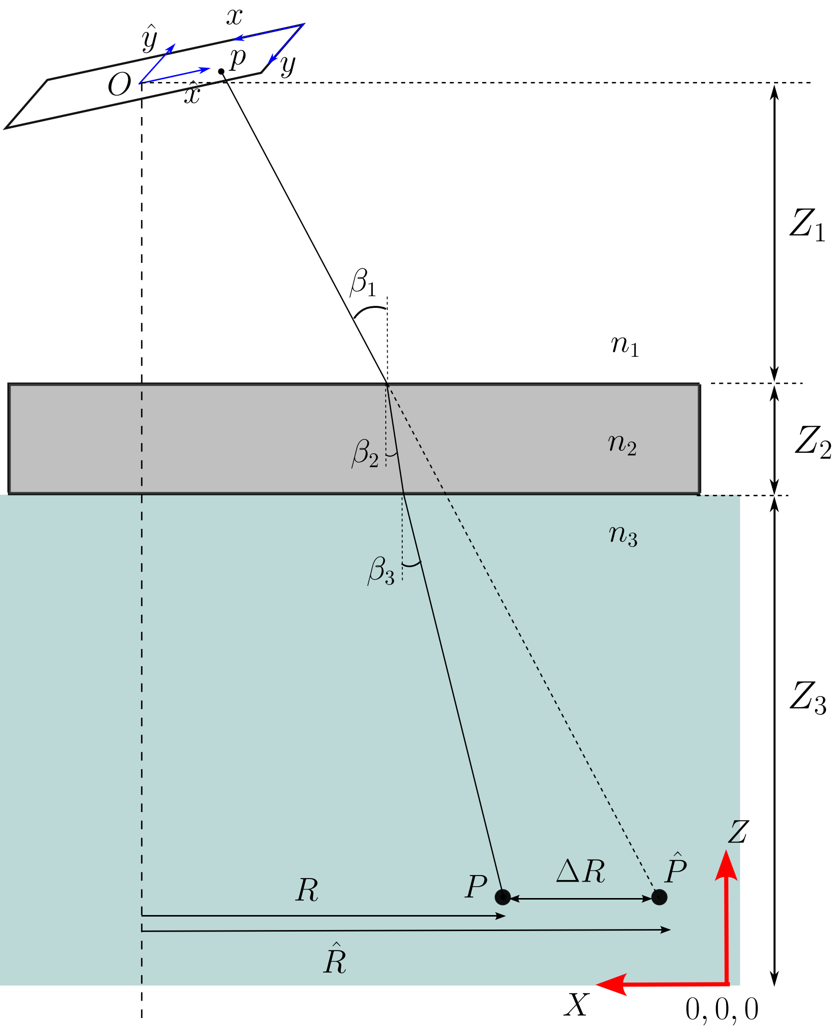

Figure 1. Multi-media correction to the Tsai model due to air-glass-water interfaces. Point $p = (x, y)$ in the image space is a projection of real point $P = (X, Y, Z)$ in the physical space or a virtual point $\hat{P} = (\hat{X}, \hat{Y}, \hat{Z})$ in the homogeneous media ($n_1 = n_2 = n_3$) model. Z_3 is the distance from the origin $(0, 0, 0)$ to the glass interface from the waterside, Z_2 is glass thickness, Z_1 is the air distance from the outer surface to the image plane center, $O = (X_0, Y_0, Z_0)$. On the image plane, the multi-media model also has a definition of image space pixel coordinates, x, y, located at the top left corner of the sensor and the metric coordinates with an imaging center O and coordinate system $\hat{x}, \hat{y}$. Vector R is a radial position of the point P in orthographic projection.

The apparent position is then calculated as

$$\hat{X} = X_0 + (X - X_0)\frac{\hat{R}}{R} \quad ,$$
$$\hat{Y} = Y_0 + (Y - Y_0)\frac{\hat{R}}{R} \quad \text{and} \quad \hat{Z} = Z. \tag{11}$$

In general, the multimedia correction comprises six model parameters: the three refraction indices and the three media thicknesses. The third and final component of the multimedia Tsai model accounts for corrections to barrel or pillow lens distortions that are especially relevant when using high magnification lenses [33]. The compensation of these effects is obtained by a set of additional parameters which non-linearly correct the 2D image coordinates,

$$\begin{aligned}
\hat{x}_i &= x_i + x_i\left(k_1 d_i^2 + k_2 d_i^4 + k_3 d_i^6\right) + p_1\left(d_i^2 + 2x_i^2\right) + 2p_2 x_i y_i, \\
\hat{y}_i &= y_i + y_i\left(k_1 d_i^2 + k_2 d_i^4 + k_3 d_i^6\right) + 2p_1 x_i y_i + p_2\left(d_i^2 + 2y_i^2\right), \\
d_i^2 &= x_i^2 + y_i^2\ .
\end{aligned} \tag{12}$$

Here, k_1, k_2, and k_3 denote radial distortion coefficients and p_1, and p_2 tangential distortion coefficients. Furthermore, to compensate for additional aberrations due to lower-quality lenses, an additional affine transformation is performed [3] with parameters $x_0, y_0, s_x, s_y, \gamma$, and δ as follows. s_x and s_y are the scaling factors that account for any difference between the physical dimensions of the pixels and the assumed square pixel dimensions, and x_0 and y_0 are the coordinates of the principal point, which is the intersection of the optical axis with the image plane,

$$\begin{aligned}\hat{x}_i &= x_0 + s_x\hat{x}_i\left(\cos\gamma\right) - s_y\hat{y}_i\left(\sin\left(\gamma+\delta\right)\right),\\ \hat{y}_i &= y_0 + s_x\hat{x}_i\left(\sin\gamma\right) + s_y\hat{y}_i\left(\cos\left(\gamma+\delta\right)\right).\end{aligned} \tag{13}$$

Thus, the third component of the multimedia Tsai model contains eleven additional model parameters.

Overall, the multimedia Tsai model contains 29 optimizable parameters per camera. Using this model in practice requires two essential processes. The forward transformation, $\mathcal{T}_M$, takes a 3D point (X, Y, Z), applies the multimedia correction to get the apparent position $(\hat{X}, \hat{Y}, \hat{Z})$, uses the collinearity equation (6) to project to image coordinates (x_i, y_i), and finally applies lens distortion correction and aberration correction. The backward transformation $\mathcal{T}_M^{-1}$ starts with image coordinates, removes lens distortion, uses the collinearity condition equation (6) to get ray direction, applies inverse multimedia correction, and intersects corrected rays from multiple cameras to obtain a particle's 3D position.

The calibration of this model requires a carefully designed process (see [9] for detailed information) that involves two steps: first, the camera position and rotation $(X_0, Y_0, Z_0, \theta_X, \theta_Y, \theta_Z)$ and interior orientation parameters (f, x_h, y_h) are determined using the collinearity condition (equation (6)). Second, the multimedia parameters $(Z_1, Z_2, Z_3, n_1, n_2, n_3, \beta_1, \beta_2, \beta_3)$ and distortion coefficients $(k_1, k_2, k_3, p_1, p_2, x_0, y_0, s_x, s_y, \gamma, \delta)$ are optimized using a bundle adjustment approach. This nonlinear optimization minimizes the RMS of the discrepancy between the projection of the calibration target using the model, $\mathcal{T}_M$ and its image captured by the camera. Notably, finding the optimal solution for this problem is a challenging task, as the non-linear components of the model render it a non-convex optimization problem that might converge to sub-optimal local minima for inappropriate initial guesses. The camera calibration model just described has been used in numerous works in the past and within many different research groups since the introduction of OpenPTV in the 1990s, for example, [12, 14, 34–40] among many others.

2.3. Polynomial Tsai model

The polynomial Tsai model uses a mixed approach that combines the pinhole camera model with a non-linear polynomial correction term $\vec{e}$. The non-linear polynomial correction is meant to account for any non-linearity in the imaging system without adhering to any physical model, similar to the approach used in [16, 41]. The advantage of this approach is that it retains information regarding the physical optical setup used in an experiment, while adhering to a simpler account of the non-linear distortions as compared to the multimedia model, yet its drawback is that one is never certain that the shape of the correction term is sufficient to fully account for all the aberrations of a given system. The polynomial Tsai model was implemented here using MyPTV software [27].The transformation from 3D physical world coordinates to 2D image coordinates in the camera i is described by the following relation,

$$\begin{bmatrix} x_i - x_h \\ y_i - y_h \\ -f \end{bmatrix} = \mathbf{R}\cdot\begin{bmatrix} X - X_0 \\ Y - Y_0 \\ Z - Z_0 \end{bmatrix} + \vec{e}\left(x_i, y_i\right). \tag{14}$$

The model parameters are X_0, Y_0, Z_0,f, $\mathbf{R}$, x_h, and y_h, being the camera position coordinates, the focal length, the camera rotation matrix described by three angle components θ_X, θ_Y, θ_Z and the two offset corrections of the imaging center. The apparent similarity to equation (6) is due to the fact that both use pinhole camera optics. The main difference between the models stems from the vector $\vec{e}$ that contains the non-linear correction terms. Here, the correction is taken as the second-order polynomial

$$\vec{e}\left(x_i, y_i\right) = \mathbf{E}\cdot\vec{P}\left(x_i, y_i\right) = \begin{bmatrix} E_{11} & E_{12} & E_{13} & E_{14} & E_{15} \\ E_{21} & E_{22} & E_{23} & E_{24} & E_{25} \\ 0 & 0 & 0 & 0 & 0 \end{bmatrix}\cdot\begin{bmatrix} x_i \\ y_i \\ x_i^2 \\ y_i^2 \\ x_i y_i \end{bmatrix}, \tag{15}$$

where E_{ij} are the polynomial coefficients stored in the polynomial coefficient matrix $\mathbf{E}$. The row E_{i3} is equal to zero because it is assumed that the focal length is not affected by the image coordinates x_i and y_i.

The polynomial Tsai model contains 19 parameters per camera. The cameras are calibrated by taking images of a calibration target and solving for the camera parameters that minimize the RMS of the discrepancy between the projection and the captured images. The minimization is performed via the numerical Nelder–Mead scheme implemented in the Scipy package [42], and it runs in separate iterations for the linear and non-linear parts of the model. Equation (14) comprises the transformation from 3D to 2D coordinates, $\mathcal{T}_M$. Therefore, given a particle whose position is (X, Y, Z), equation (14) can be used to calculate its camera coordinates, that is, its projection on the camera sensor (x_i, y_i) of the camera i. To obtain the inverse transformation, $\mathcal{T}_M^{-1}$, equation (14) is rearranged to define a line of sight in the 3D coordinates, connecting the center of the camera (X_0, Y_0, Z_0) and the position of the particles (X, Y, Z). If a particle is seen by two or more cameras simultaneously, we can estimate its 3D position by the intersection (or the point that most closely approximates the intersection) of such lines of sight. This operation comprises the inverse transformation, $\mathcal{T}_M^{-1}$. This approach has been used in several recent works that have investigated Lagrangian statistics of turbulent flows [43, 44].

2.4. Soloff polynomial model

The Soloff polynomial model, implemented here in proPTV, uses a polynomial projection model that takes 3D physical world coordinates, (X, Y, Z), and outputs the 2D camera coordinates (x_i, y_i) of camera i, thus comprising the forward transformation $\mathcal{T}_M$. The mapping function, equation (16), is based on the Soloff model [15], which uses a 3rd order polynomial in X and Y and a 2nd order polynomial in the depth direction of the camera view, Z:

$$\begin{bmatrix} x_i \\ y_i \end{bmatrix} = \mathbf{A}_i\cdot\vec{S}\left(X,Y,Z\right). \tag{16}$$

Here, the matrix $\mathbf{A}_i$ contains the polynomial coefficients for a given camera i, comprising a total of 19×2 individual coefficients,

$$\mathbf{A}_i = \begin{bmatrix} a_{0x}^{(i)} & a_{1x}^{(i)} & a_{2x}^{(i)} & \cdots & a_{18x}^{(i)} \\ a_{0y}^{(i)} & a_{1y}^{(i)} & a_{2y}^{(i)} & \cdots & a_{18y}^{(i)} \end{bmatrix}. \tag{17}$$

The vector $\vec{S}$ stores the variables of the polynomial mapping function based on the Soloff model,

$$\vec{S}(X,Y,Z) = \left[1, X, Y, Z, X^2, Y^2, Z^2, XY, YZ, XZ, X^3, Y^3, X^2Y, X^2Z, XY^2, Y^2Z, XZ^2, YZ^2, XYZ\right]^{\mathrm{T}}. \tag{18}$$

The polynomial coefficients of each camera, $\mathbf{A}_i$, are individually estimated by minimizing the following loss function of the sum of squares of the discrepancy between the projection of the calibration target (equation (16)) and the estimated marker centroids on the camera i,

$$\mathcal{L}_i = \sum_{k=1}^{N} \left|\left| \begin{bmatrix} x_i \\ y_i \end{bmatrix}_k - \mathbf{A}_i \cdot \vec{S}_k \right|\right|^2. \tag{19}$$

The Soloff model in equation (16) is not invertible analytically, so a numerical approach is taken to obtain the backward transformation $\mathcal{T}_M^{-1}$. This problem is solved by an iterative reconstruction algorithm, which is explained in [17] in more detail. In summary, a gradient descent algorithm is used that estimates the correction $\vec{h}$ to an initial 3D position, which is always in the middle of the measurement domain, until convergence to floating precision is reached in the re-projection error of the 3D position onto the camera images of multiple cameras. Usually, five iterations are enough. Following the concept of [45], the gradient descent problem is stated as an iterative multi-camera optimization problem at iteration $n+1$ by:

$$\vec{X}_{n+1} = \vec{X}_n - \vec{h}_n \quad , \quad \vec{h}_n = \mathbf{G}_n^{-1}\left(\vec{X}_n\right) \cdot \vec{g}_n\left(\vec{X}_n\right), \tag{20}$$

with the Jacobi matrix of the Soloff projection $\mathbf{G}$ for all N_c cameras at iteration n

$$\mathbf{G}_n = \begin{pmatrix} \mathbf{A}_1 \cdot \partial_X \vec{S}_n & \mathbf{A}_1 \cdot \partial_Y \vec{S}_n & \mathbf{A}_1 \cdot \partial_Z \vec{S}_n \\ \mathbf{A}_2 \cdot \partial_X \vec{S}_n & \mathbf{A}_2 \cdot \partial_Y \vec{S}_n & \mathbf{A}_2 \cdot \partial_Z \vec{S}_n \\ \vdots & \vdots & \vdots \\ \mathbf{A}_{N_c} \cdot \partial_X \vec{S}_n & \mathbf{A}_{N_c} \cdot \partial_Y \vec{S}_n & \mathbf{A}_{N_c} \cdot \partial_Z \vec{S}_n \end{pmatrix}, \tag{21}$$

and the reprojection error $\vec{g}$ for all N_c cameras at iteration n

$$\vec{g}_n = \begin{pmatrix} \mathbf{A}_1 \cdot \vec{S}_n - \vec{x}_1 \\ \mathbf{A}_2 \cdot \vec{S}_n - \vec{x}_2 \\ \vdots \\ \mathbf{A}_{N_c} \cdot \vec{S}_n - \vec{x}_{N_c} \end{pmatrix}. \tag{22}$$

The size of matrix $\mathbf{G}$ and vector $\vec{g}$ depends on the number of cameras used for the reconstruction. When only a single camera is used, a 3D position along the line of sight of that camera is estimated for the given image coordinate $\vec{x}_i = (x_i, y_i)$. The usage of two or more cameras results in the reconstruction of a concrete 3D particle position $\vec{X} = (X, Y, Z)$ and thus inverts the Soloff projection function.

Overall, the Soloff polynomial method is a flexible and simple calibration method with a high degree of non-linear correction, ideal for multi-media experiments because it is just a fit between the 3D world and its 2D representation on a camera. However, its main drawback is that the physical camera parameters, such as the camera position of the imaging system, are not retained in the calibration, as these parameters do not carry any physical information. Usually in PTV and with proPTV, these parameters are not needed, so it is just a drawback in other applications. Interestingly, the main contribution to the calibration error of the Soloff model comes from uncertainties in the position of the 3D markers, which are related to the experimental procedure of moving the plate through the volume. This is fundamentally different from model-based calibrations, such as those using the Tsai model, because the calibration models attempt to model the optics of a camera device, which are always approximations to the real world, and the model parameters contain various error contributions, for example from lens errors, depth of field blur, alignment to the experiment, etc. The Soloff polynomial model and its application to PTV is tested successfully in [17, 23].

2.5. Inverse Soloff polynomial model

The last calibration model that we consider is a hybrid approach that combines features of the Soloff model used in section 2.4 and the pinhole camera approach used in sections 2.2 and 2.3. As shown in the previous section, an inherent difficulty of the Soloff polynomial model is that it is not invertible because the polynomials in equation (16) are non-linear. On the other hand, an inherent difficulty of the two modified Tsai models introduced before is that the process used to find optimal camera parameters is challenging as it involves solving a non-convex optimization problems with numerous parameters. To alleviate these issues, we searched for a hybrid calibration model that relies on the advantages of all methods described above to overcome their limitations, a search that had culminated in the inverse Soloff polynomial model described as follows.

For the forward transform from 3D world coordinates to 2D camera coordinates, $\mathcal{T}_M$, the new model uses exactly the same method as the Soloff model, namely, equation (16). Thus, the calibration procedure for $\mathcal{T}_M$ uses the same least squares minimization scheme as described in section 2.4. This is because the Soloff model can be easily applied in the forward direction (projection from 3D to 2D). For the inverse transformation, $\mathcal{T}_M^{-1}$, the new model uses the laws of the pinhole camera optics. In particular, each camera is associated with an optical center (which does not necessarily coincide with the camera's physical position), and each 2D image point is associated with a line of sight whose orientation is defined through polynomials of order 3. Specifically, intrinsic to this model is the assumption that each 2D camera position (x_i, y_i) is associated with a (linear) line of sight and that all lines of sight cross at some point in the 3D physical world, $\vec{O} = (X_0, Y_0, Z_0)$. Therefore, points along the 3D line of sight are given by

$$\vec{l}_i(x_i, y_i, \mu) = \vec{O}_i + \mu \vec{U}_i(x_i, y_i) \ , \tag{23}$$

where μ is a free parameter that determines the position along the line and $\vec{U}_i$ represents the unit vector associated with each 2D image coordinate of the camera i, defined as

$$\vec{U}_i(x_i, y_i) = \mathbf{B}_i \cdot \vec{u}(x_i, y_i)^{\mathrm{T}} \ . \tag{24}$$

Here, the matrix $\mathbf{B}_i$ stores the polynomial coefficients of the camera i and the vector $\vec{u}$ defines the polynomial based on the 2D camera coordinates.

$$\mathbf{B}_i = \begin{bmatrix} b_{0X}^{(i)} & b_{1X}^{(i)} & b_{2X}^{(i)} & \cdots & b_{9X}^{(i)} \\ b_{0Y}^{(i)} & b_{1Y}^{(i)} & b_{2Y}^{(i)} & \ldots & b_{9Y}^{(i)} \\ b_{0Z}^{(i)} & b_{1Z}^{(i)} & b_{2Z}^{(i)} & \ldots & b_{9Z}^{(i)} \end{bmatrix} \tag{25}$$

$$\vec{u}(x_i, y_i) = \left(1, x_i, y_i, x_i^2, y_i^2, x_i y_i, x_i^3, y_i^3, x_i^2 y_i, x_i y_i^2\right)^{\mathrm{T}} . \tag{26}$$

In total, each camera in the inverse Soloff polynomial model is characterized using the 19×2 coefficients stored in matrix $\mathbf{A}_i$ for the forward transformation $\mathcal{T}_M$. The backward transformation $\mathcal{T}_M^{-1}$ includes three coordinates of the optical center, $\vec{O}_i$, plus the 10×3 coefficients stored in matrix $\mathbf{B}_i$. This gives a total of 71 parameters per camera, but they are divided into 38 and 33 parameters for each transformation direction, respectively. The calibration parameters in the forward direction are calculated in the same way as described for the Soloff model in section 2.4. The model parameters in the backward direction are determined by associating a line of sight for each marker position, by numerically searching for two 3D positions, that when projected using $\mathcal{T}_M$ fall on the same 2D image coordinates of the marker centroids. Then, we estimate (X_0, Y_0, Z_0) as the point that best approximates the crossing of all lines of sight as the camera position in 3D world coordinates. Finally, we find the optimal solution for $\mathbf{B}_i$ by least squares optimization. All these steps were implemented in MyPTV [27] by using the Scipy package [42]. This is the first work to describe the inverse Soloff polynomial model and it was not tested before.

3. Experimental apparatus

The calibration models are evaluated using raw calibration images taken during the calibration of an experimental PTV setup designed to study Rayleigh–Bénard convection in a cubic cell filled with water [23]. The experimental setup is optically complex, involving transitions between several media with different refractive indices (air, glass, and water), which is typical for laboratory PTV experiments. Figure 2(a) shows a picture of the experimental apparatus. The cubic cell has an internal side length of $L = 300$ mm and consists of four 8 mm thick glass sidewalls for optical access to the measurement volume, glued together with silicone and glued to a black anodized aluminum plate heated from below with an electric heating mat. A black anodized aluminum cooling cover is placed on top of the cell. Four PCO Edge 5.5 cameras with a pixel size of 6.5×6.5 µm, a resolution of 2560×2160 pixels and a sensor diagonal of 21.8 mm are mounted approximately 1 m from one of the outer glass sidewalls of the cube to study the motion of seeding particles in a PTV measurement, and LED arrays are placed on the side at 90 ° to the cameras, to illuminate the interior of the cell. Each of the four cameras was mounted with a 21 mm objective.

The camera system is calibrated to the coordinate system shown in figure 2(b) using a square solid calibration plate made of aluminum with 19×19 imprinted marker dots. The diameter of each marker point is $d = 1.5$ mm and they are separated by $D = 15$ mm in the X–Y plane. The origin of the coordinate system is placed on the inside of the cell in the lower left corner from the camera view farthest away from the cameras. Calibration involves removing the cooling lid and placing a socket on the top of the cell to which the calibration plate can be attached. The calibration plate is moved through the cell at five depth positions at approximately $Z \in \{274, 212, 150, 88, 26\}$ mm and a distance of $\Delta Z = 62$ mm is achieved between the marker positions. Figure 3 shows the calibration images of camera 4 for all depth positions of the calibration target.

4. Model comparison

In this section, we compare the four calibration models introduced in section 2 based on their 2D and 3D calibration errors. The experiment described in section 3 provides us with a marker list including the 3D marker positions and their 2D marker centroid for all four cameras. The 3D positions of the markers are approximated and given based on the convection of our coordinate system. The 2D positions are estimated using the proPTV marker centroid search tool on the camera images of the calibration target shown in figure 3. The unchanged marker list is used to calibrate each of the four camera models. In what follows, we report three test cases to compare the 2D and 3D calibration errors of the models. First, all marker plate positions at $Z \in \{274, 212, 150, 88, 26\}$ mm shown in figure 4(a) are used to estimate the calibration parameters of each model. The second test case compares the models in their 'interpolation accuracy', namely their ability to infer the 3D positions of points that do not lie on the locations of the markers used for the calibration. This is achieved by using the calibration markers only at $Z \in \{274, 150, 26\}$ mm (figure 7(a)) to calibrate the different models and then estimating the positions of the markers placed at all the positions of the plate. The third case refers to the 'extrapolation accuracy' of the models using only marker planes with $Z \in \{212, 150, 88\}$ mm (figure 10(a)) for calibration while calculating the calibration errors on the marker positions of all planes. In the following, most of the time, we refer to an averaged calibration error in 2D and 3D calculated by averaging the error magnitude along the markers per plane. The average 2D and 3D calibration errors are denoted by $\langle \delta_{M,i}^{2D} \rangle_{XY}$ and $\langle \delta_M^{3D} \rangle_{XY}$, respectively. The individual components of the 3D calibration error in each direction are indicated by: $\delta_X^{3D}, \delta_Y^{3D}, \delta_Z^{3D}$. Note that the Kolmogorov length of

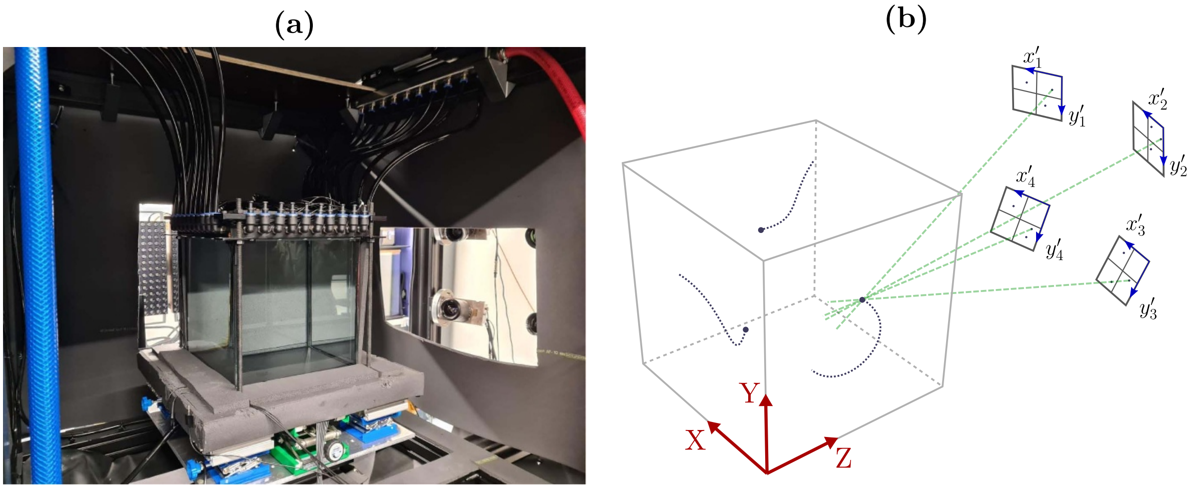

Figure 2. (a) Photograph of the Rayleigh–Bénard apparatus, comprising a cubic cell filled with water. Four cameras observing the flow are shown to the right and side, and an LED array is placed on the side wall of the cube to the left of the cameras. (b) Definition of coordinate systems: capital letters X,Y,Z are used for the 3D physical world with its origin at the lower left rear corner from the camera viewpoint. Lowercase letters x_i, y_i with index i are used for the pixel coordinate systems in image space with top left as origin, for $i = 1,\ldots,N_c$ cameras, typically $N_c = 4$. Reproduced with permission from [23]. © 2024 The Author(s). Published by Informa UK Limited, trading as Taylor & Francis Group. CC BY-NC-ND 4.0

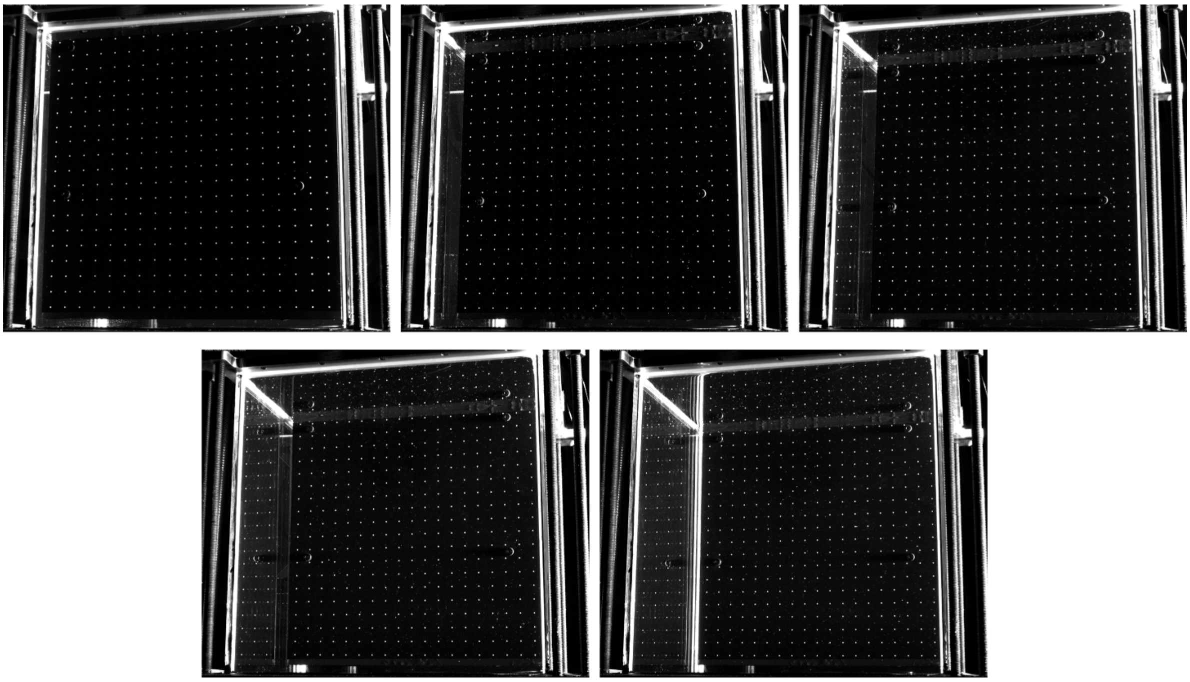

Figure 3. The calibration target used to evaluate the models in this work, shown at five depth positions with $Z \in \{274, 212, 150, 88, 26\}$ mm imaged by camera 4.

the flow studied with the experimental setup used here is about $\eta = 0.5$ mm. This will help characterize the order of magnitude of the 3D calibration error.

4.1. All markers

The 3D marker points used for calibration and the resulting average 3D calibration errors per plane for each model are shown in figures 4(a) and (b), respectively. Furthermore, component-wise 3D calibration errors per marker point for each model are shown in figure 5. The average 2D calibration errors per camera for each plane and each model are shown in figure 6. The average 3D calibration error is less than 1 mm for all planes and all models, but only the Soloff and multimedia Tsai model provide errors always below the Kolmogorov length scale given by $\eta = 0.5$ mm and thus both methods could reconstruct the flow at its smallest length scale. The Soloff model provides the lowest average 2D and 3D calibration error compared to the other models.

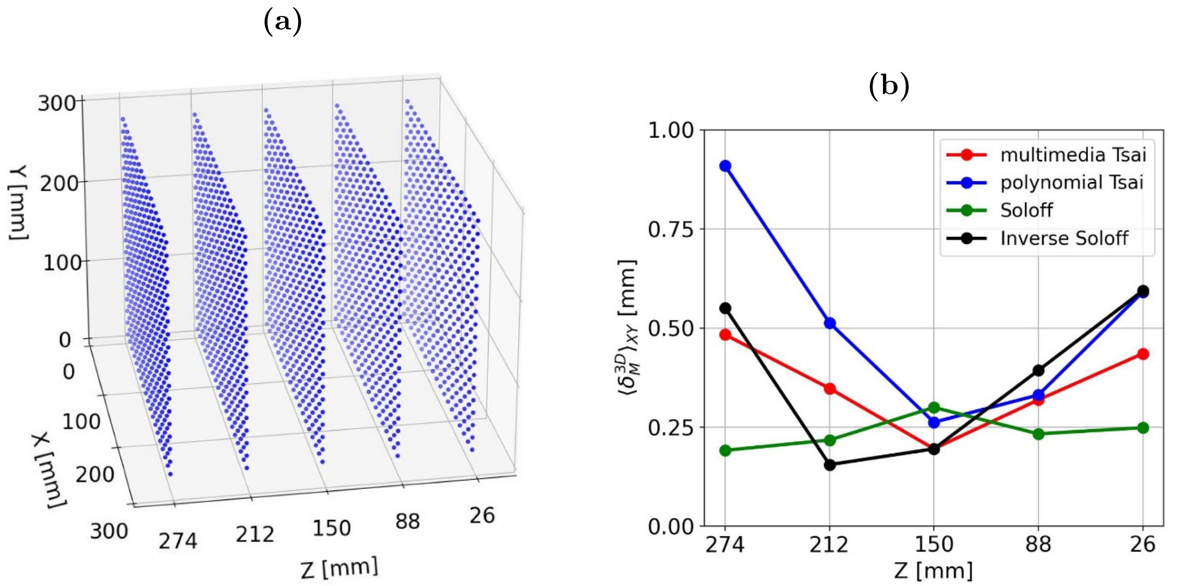

Figure 4. (a) The 3D marker positions used to calibrate each model. (b) Averaged 3D calibration error of the marker points of four calibration models along each plane position.

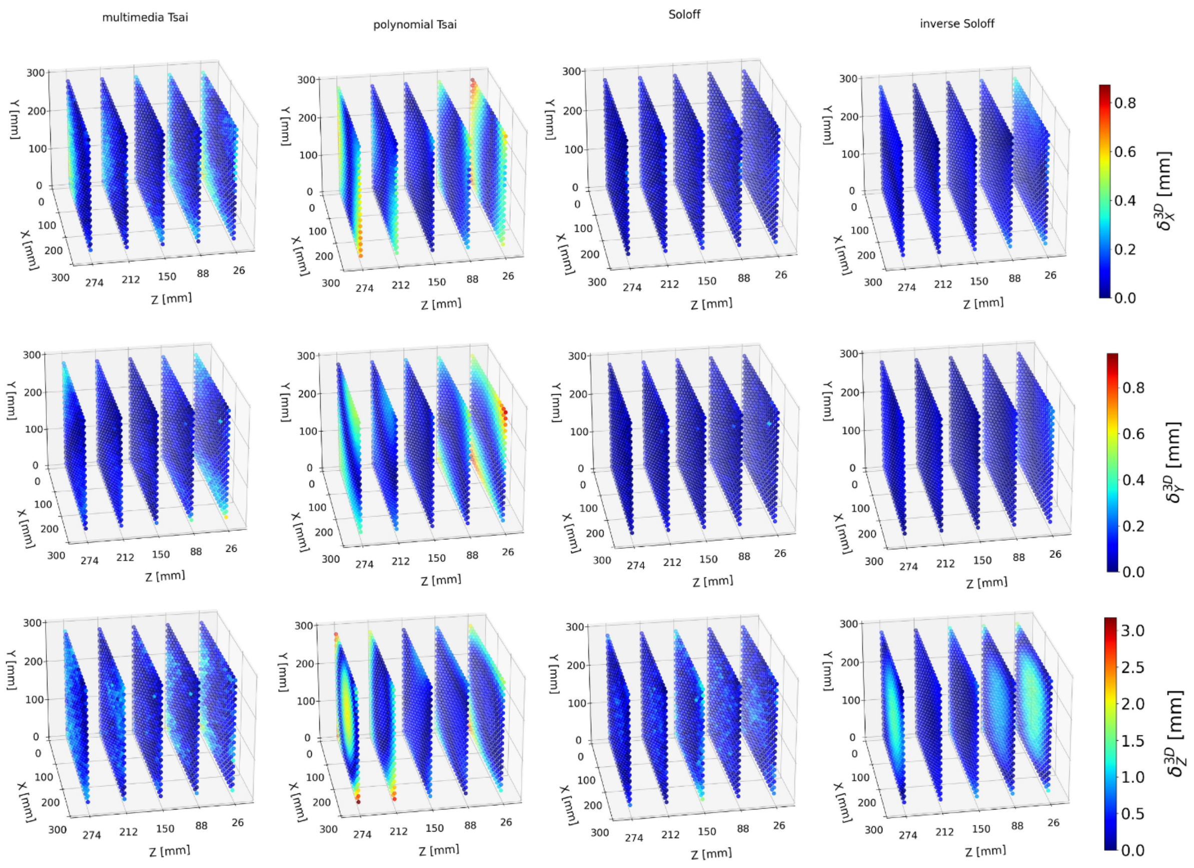

Figure 5. Components of the 3D calibration error of all models (rows) and the three directions. The components of the calibration error: δ_X^{3D} (first column), δ_Y^{3D} (second column), and δ_Z^{3D} (third column), are shown using the respective color maps.

Furthermore, for all but the Soloff model, the 3D calibration error tends to have larger values on the outside of the calibrated volume, while the Soloff model provides result with a uniform distribution of the similar 3D errors throughout the calibration markers. Figure 5 shows that the calibration error in the Z direction of the coordinate system contributes the most to the overall 3D error and is much higher than the errors in the X or Y direction. This is mainly because there are more

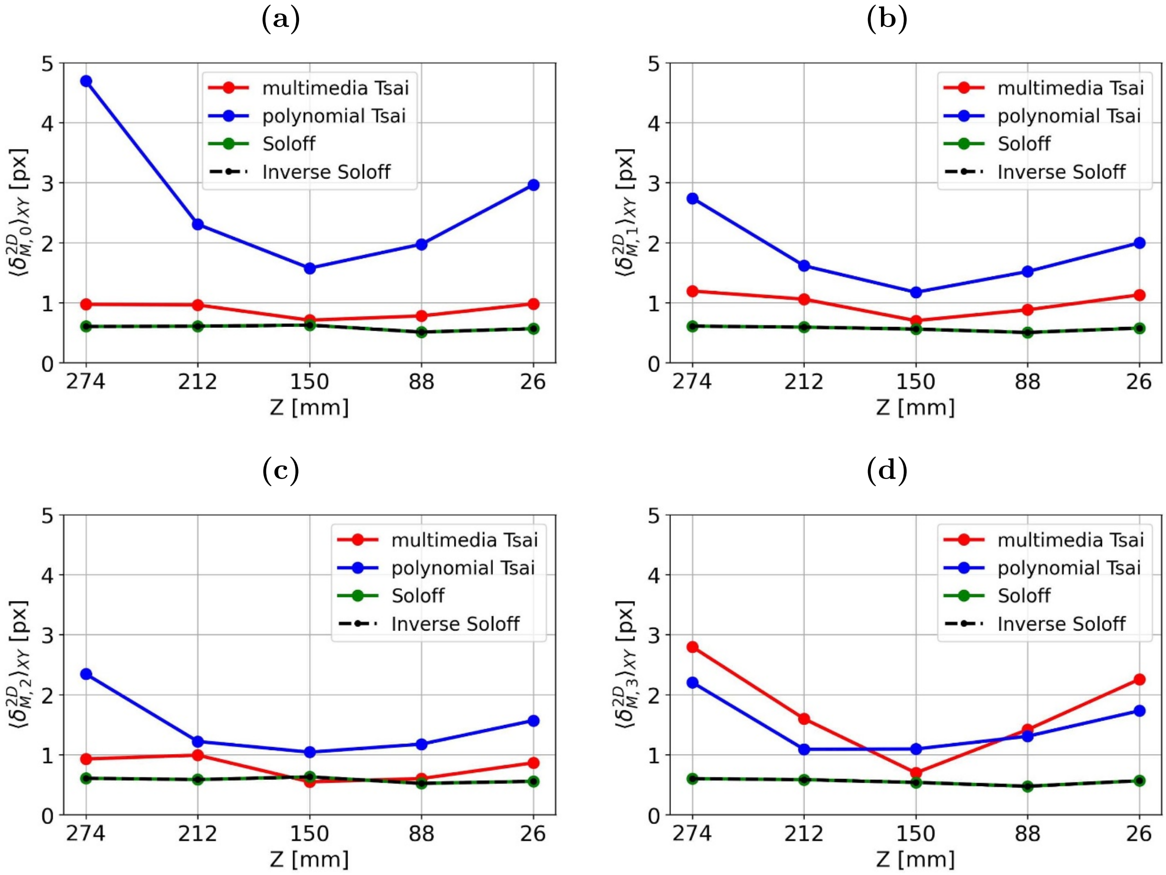

Figure 6. The averaged 2D calibration error using all markers for calibration of all camera models with respect to each of the four cameras: (a) camera 1, (b) camera 2, (c) camera 3, (d) camera 4.

calibration markers given in the X–Y plane than in the depth direction Z and also the positional uncertainty of determining the marker coordinates in X and Y is easier because their distance is fixed along the plane. The plates move through the volume and are fixed in certain places with screws, which provides some experimental uncertainty in the actual position of the plates Z. A tilt in the orientation of the plates from one position to the other is not expected with our calibration device. The higher calibration errors obtained in the depth direction are a common occurrence in PTV experiments. The highest 3D calibration errors are seen to occur for the polynomial Tsai and the inverse Soloff method at the extremities of the calibration region. The common feature for the two is that they use quadratic non-linear corrections, which may not be enough to express the 2D–3D correspondence near the glass sidewalls.

4.2. Interpolation

The 3D marker points used for calibration in the interpolation comparison and the resulting averaged 3D calibration errors for each model are shown in figures 7(a) and (b), respectively, and the distribution of the various components of the 3D calibration errors are shown in figure 8. The average 2D calibration errors per camera for each plane and each model are shown in figure 9.

Figure 7(b) shows two different behaviors of the calibration errors for the four models. The multimedia and the Soloff model show the same error distribution and both have their maximum error at the marker plane with $Z = 212$ mm which is one of the interpolation positions. The error in this plane of both models is above the Kolmogorov length scale of $\eta \approx 0.5$ mm but smaller than 1 mm, which is still enough to reconstruct small structures in the flow. For the two models, the errors on all other four plane positions are below the Kolmogorov length scale and thus provide good reconstruction results. On the other hand, the polynomial Tsai and the inverse Soloff model show a completely different behavior. Both of their average 3D calibration errors have a V shape and are maximal in the outer plane positions and minimal at the middle plane. The same picture is found by comparing the individual 3D calibration error components, see figure 8. The average 2D calibration errors per camera for each plane and each model are shown in figure 9. Expect for the plane at $Z = 212$ mm the Soloff method provides the best results with an average error always about 0.5 pixels. The polynomial Tsai model shows strong reprojection errors of up to 5 pixels in the first camera. Overall, the multi-media model shows the

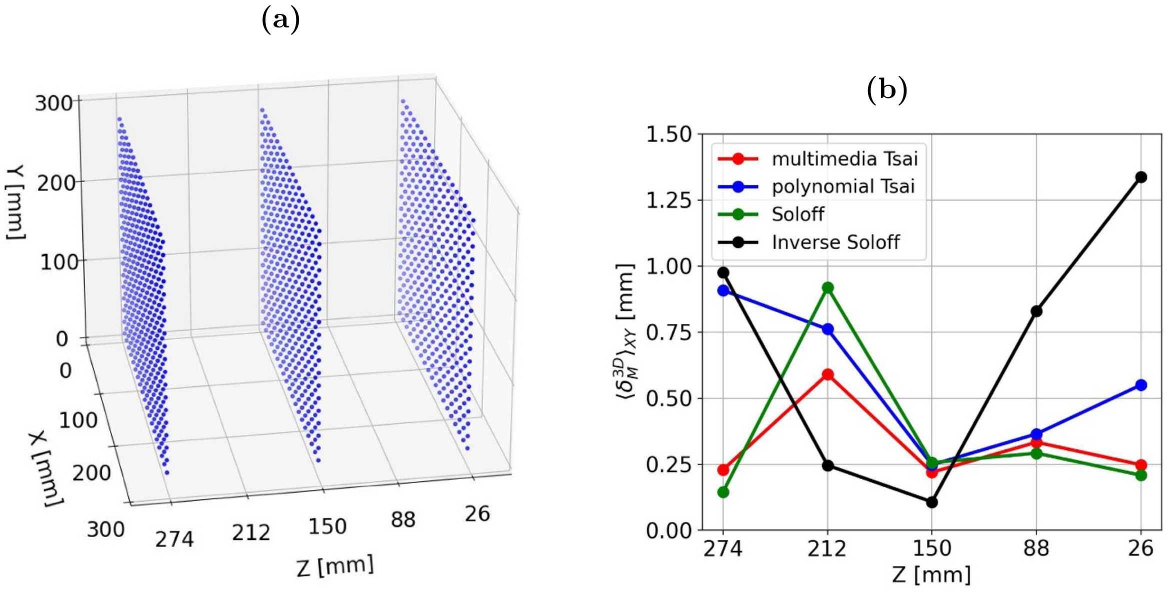

Figure 7. (a) The 3D marker positions used to calibrate each model in the interpolation case. (b) Averaged 3D calibration error of the marker points of four calibration models along each plane position.

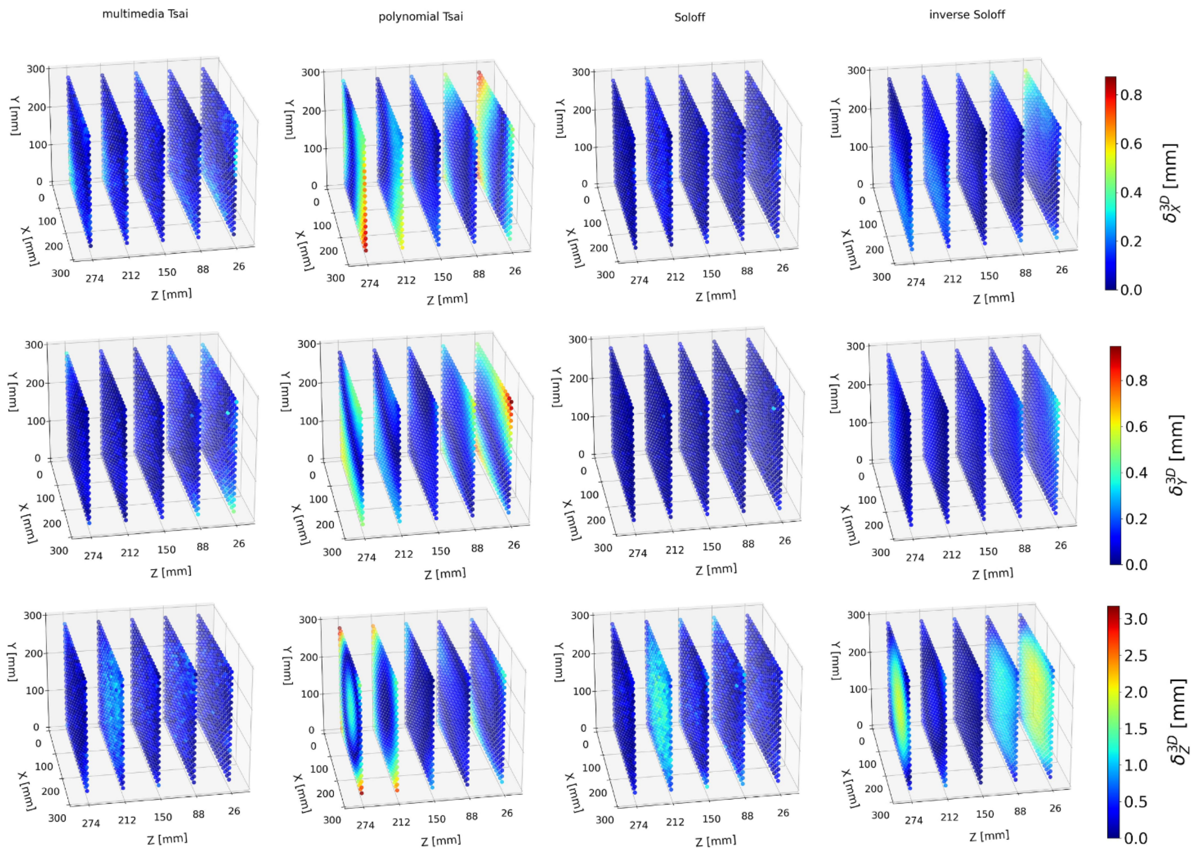

Figure 8. Components of the 3D calibration error of all models (rows) and the three directions for the interpolation case using only planes with $Z \in \{274, 150, 26\}$ mm for calibration. The components of the calibration error: δ_X^{3D} (first column), δ_Y^{3D} (second column), and δ_Z^{3D} (third column), are shown using the respective color maps.

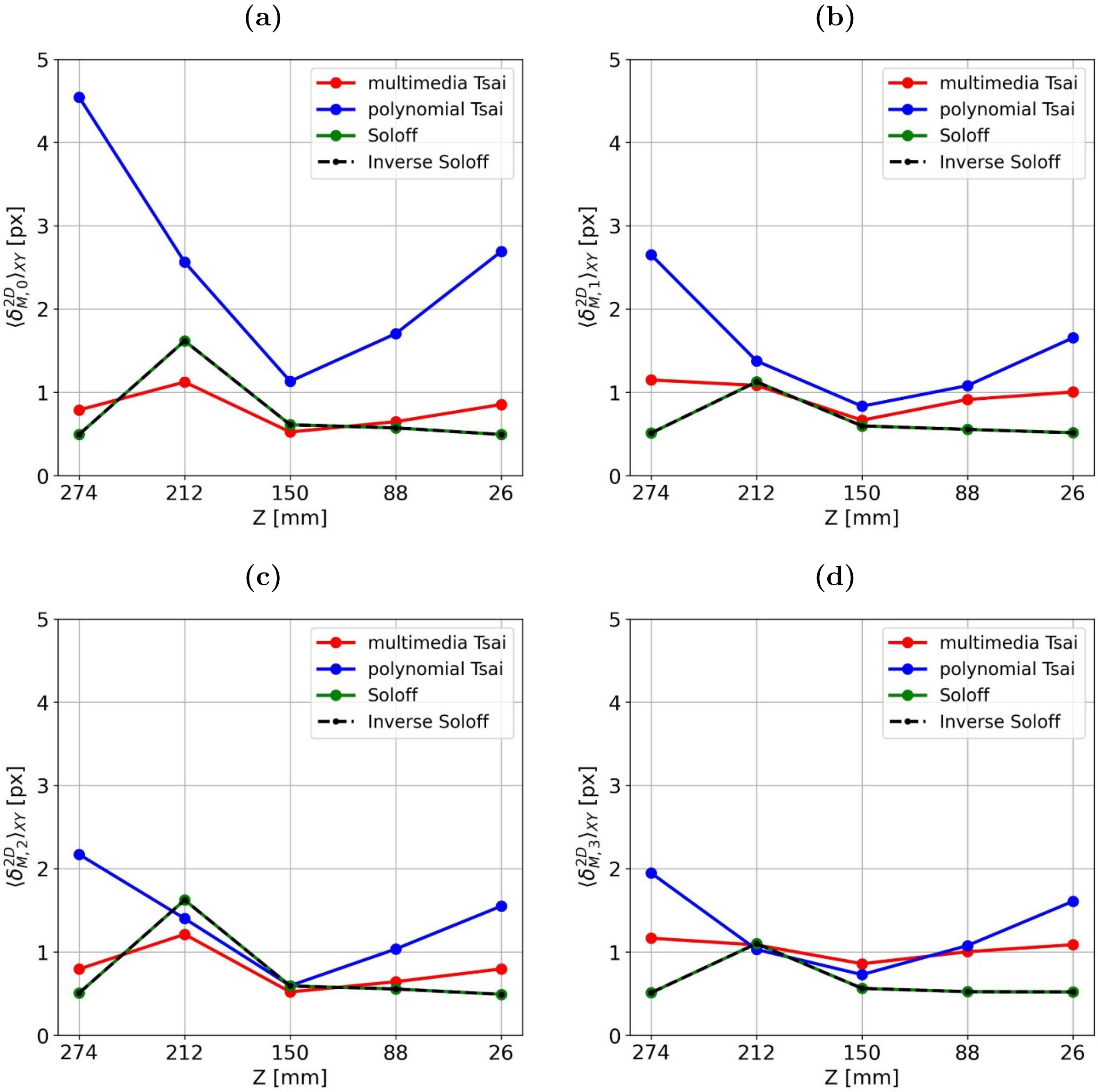

Figure 9. The averaged 2D calibration error in the interpolation case using only planes with $Z \in \{274, 150, 26\}$ mm for calibration of all camera models with respect to each of the four cameras: (a) camera 1, (b) camera 2, (c) camera 3, (d) camera 4.

best performance together with the Soloff method except for $Z = 212$ mm where the Soloff method provides a higher error.

4.3. Extrapolation

The 3D marker points used for the calibration in the extrapolation comparison and the resulting averaged 3D calibration errors for each model are shown in figures 10(a) and (b), respectively, and the distribution of the various components of the 3D calibration errors are shown in figure 11. Except for the first plane position at $Z = 274$ mm, the 3D calibration errors of all models are always below the Kolmogorov length scale of about 0.5 mm and good reconstruction results can be expected. At the first plane position at $Z = 274$ mm, which is also one of the extrapolation planes, all models have a higher calibration error, but most dramatically for the Soloff method with 2.5 mm. The components of the 3D calibration error, shown in figure 11, provide a similar picture in addition to the higher errors of the polynomial Tsai and the inverse Soloff method near the outside of the calibrated volume, as we discovered earlier. The average 2D calibration errors per camera for each plane and each model are shown in figure 12. Expect for the plane at $Z = 274$ mm the Soloff model provides the best results with an average error at the given planes always of about 0.5 pixels. The polynomial Tsai model shows reprojection errors always above 1 pixel for all cameras. Overall, the Soloff model shows the best performance in the comparison of 2D and 3D calibration errors except for the plane at $Z = 274$ mm where the Soloff method provides the highest error.

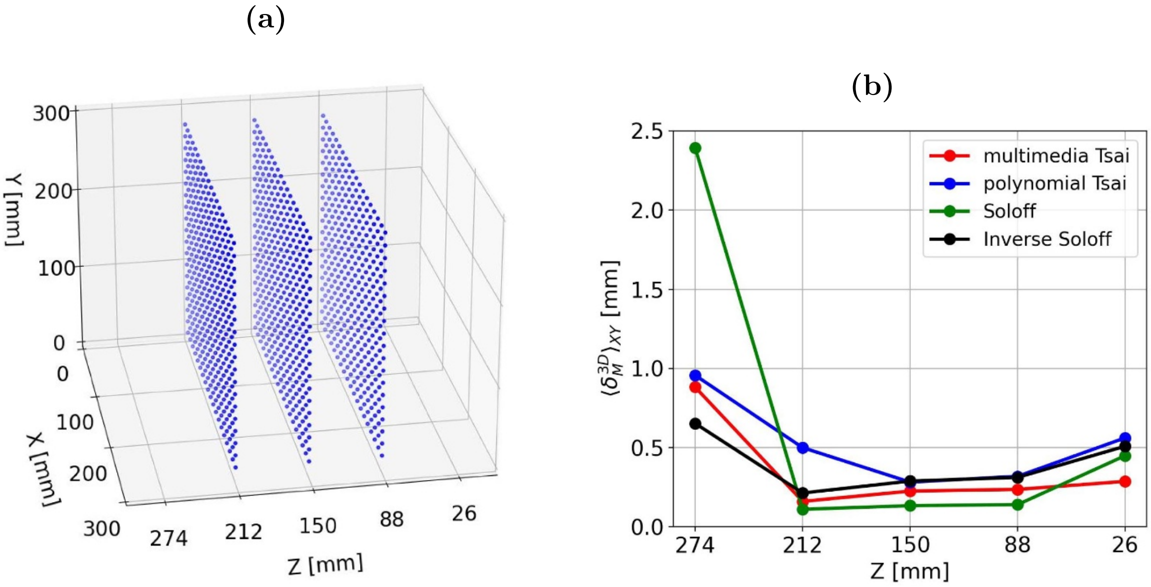

Figure 10. (a) The 3D marker positions used to calibrate each model in the extrapolation case. (b) Averaged 3D calibration error of the marker points of four calibration models along each plane position.

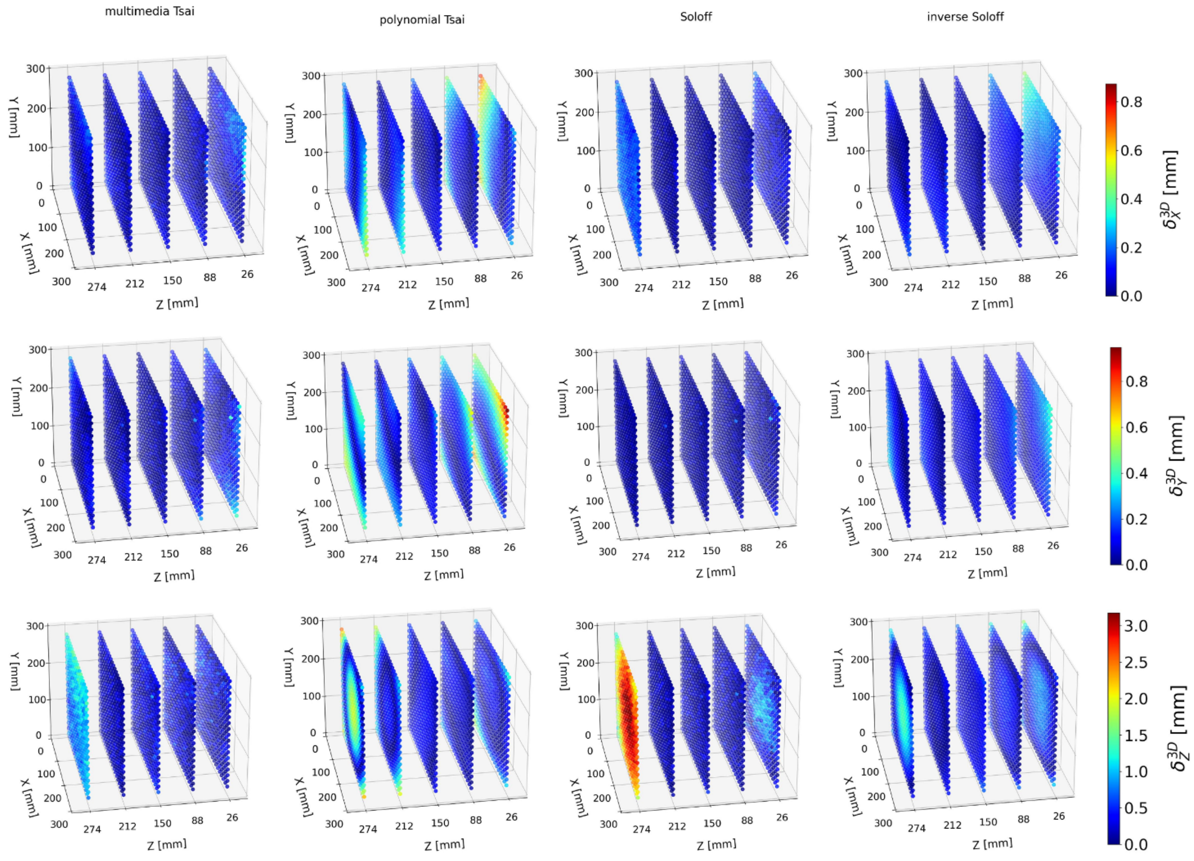

Figure 11. Components of the 3D calibration error of all models (rows) and the three directions for the extrapolation case using only planes with $Z \in \{212, 150, 88\}$ mm for calibration. The components of the calibration error: δ_X^{3D} (first column), δ_Y^{3D} (second column), and δ_Z^{3D} (third column), are shown using the respective color maps.

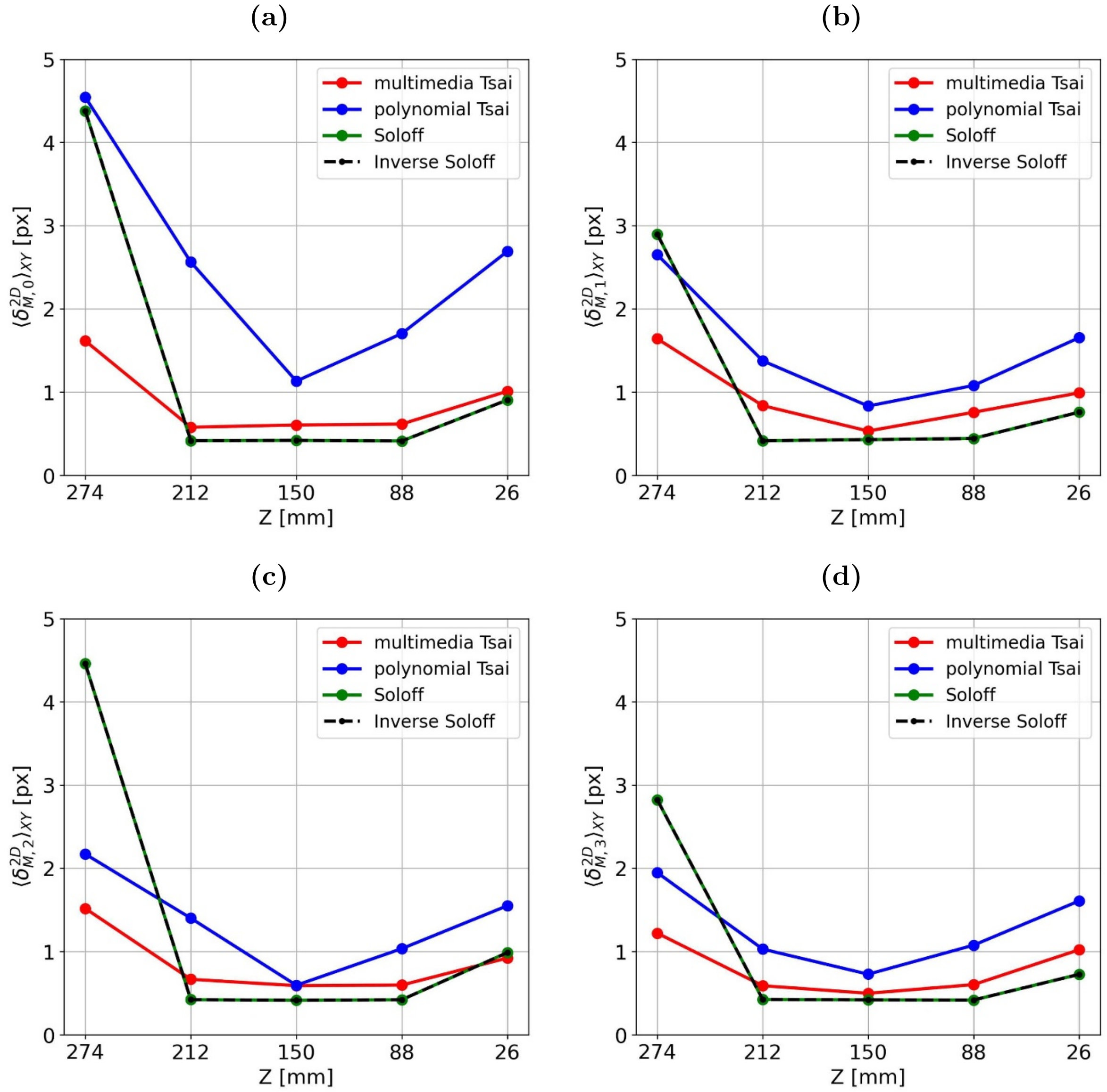

Figure 12. The averaged 2D calibration error in the extrapolation case using only planes with $Z \in \{212, 150, 88\}$ mm for calibration of all camera models with respect to each of the four cameras: (a) camera 1, (b) camera 2, (c) camera 3, (d) camera 4.

5. Conclusion

In this work, we investigate and compare four different camera calibration models used in PTV with respect to their 2D and 3D calibration errors on an optically complex experimental setup. No post-processing or additional error minimization as in volumetric calibration is performed in order to understand how the models themselves behave and what are the most important error sources in realistic experiments in different test cases, including interpolation and extrapolation tasks. Note that volumetric calibration is recommended prior to any PTV processing. In general, camera calibration models are divided into two categories: models that attempt to model the optics of a camera (Tsai models) and models that rely purely on a mathematical fit between the 2D–3D correspondence of a camera (Soloff model). Camera models that model the optics of a camera, such as the multimedia or polynomial Tsai model, provide the user with useful camera parameters such as focal length, camera positions, etc but they are analytical models and cannot be used to model the optics of a camera, but they are analytical models and cannot be used for all possible setups, e.g. the multimedia Tsai model needs to be modified in different scenarios, e.g. when the geometry changes or curved glass walls cover the experiment as in thick cylindrical tubes [30–32], and furthermore the optimization of camera parameters relies heavily on a good initial guess, which often makes it difficult to calibrate a foreign camera setup using shared measurement data from experiments that may no longer be available. On the other hand, polynomial-fit calibration models like the Soloff model provide a fast and easy method to obtain camera calibration parameters because a simple least-square optimization using the 2D–3D correspondence of the calibration marker points is enough to calibrate the system. The method is by itself generalized and can be used for all possible

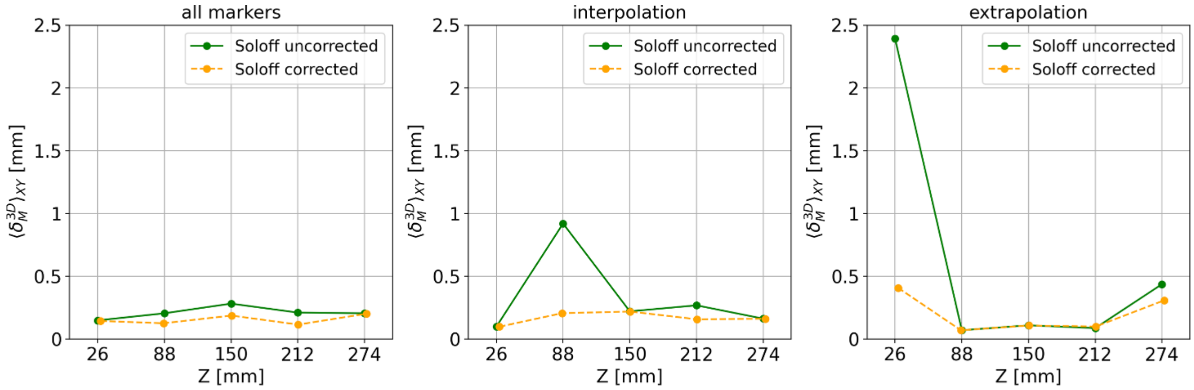

Figure 13. 3D calibration error of the Soloff polynomial for all three test cases as a green dotted line and the 3D calibration error of the Soloff polynomial by changing the Z position of each plate by a small amount from $Z \in \{26, 88, 150, 212, 274\}$ mm to $Z \in \{28.8, 87.15, 150.45, 212.4, 276\}$ mm during calibration.

setups. However, the Soloff model is not invertible analytically and it returns calibration parameters which are not physically meaningful and information like the focal length or camera position are lost. There are many error sources which limit the precision of the camera calibration using a certain model, for example: depth of field and blurred imaging errors, marker centroid detection uncertainties, lens errors, underestimated higher non-linear correction factors, inaccurate estimation or guess of the 3D marker positions. The latter mainly contributes to the calibration error using the Soloff model. This is verified by simply changing the given Z position [mm] of each plate by a small amount from $Z \in \{26, 88, 150, 212, 274\}$ mm to $Z \in \{28.8, 87.15, 150.45, 212.4, 276\}$ mm and the resulting averaged 3D calibration errors for the three cases decreases drastically, as it is shown in figure 13. Also, the unsymmetrical error shape, e.g. in the case of extrapolation at marker $Z = 26$ mm and $Z = 274$ mm, is now symmetrical. Therefore, it is recommended to use the Soloff method if one is able to control the marker movement precisely in the experiment, if one knows all 3D marker positions, and if one is not interested in the camera position or camera-related parameters at all. The uncertainty in the Z position of the marker plates contributes most to the Soloff model because it is a fit of the 2D–3D correspondence and other errors besides the negligible centroid estimation error cannot play a role, which is different for the model-based Tsai calibration methods. The polynomial order of the Soloff model is another point of consideration, but increasing the order of the polynomial requires observing the marker plane at more marker planes, and as we have seen, the position of the marker plate in depth may not be precisely estimable in experiments and will build up a high error, which is even more drastic for higher order polynomials. It is recommended to use the minimum polynomial degree in all directions which are still able to cover all non-linear corrections needed in the imaging process.

Although the camera models studied in this work use different approaches, they are based on a fundamental formulation presented in section 2. Based on this formulation, it is crucial to evaluate both the 2D projection calibration error and the 3D reconstruction calibration error to fully understand the accuracy of each camera model. Both properties are compared for three cases, including the use of all marker planes for calibration and an interpolation and extrapolation case using only three of the five marker planes. The most realistic case is the use of all five marker planes, which gives the best results. In this case, the Soloff and the multimedia model provide 3D calibration errors always below the smallest length scale in the studied RBC convection, which is the Kolmogorov length $\eta \approx 0.5$ mm, and good reconstruction results can be expected; see figure 5. The inverse Soloff model and the polynomial Tsai model show higher errors, up to a maximum error of 1 mm, which is still good enough to reconstruct small scales in the flow. Comparing the 2D calibration errors, the Soloff method shows a constant error of less than 0.5 pixels for all cameras; see figure 6. All other models show higher 2D reprojection errors, which also vary from camera to camera, suggesting that model-based calibrations and their optimization are highly dependent on initial conditions and some lens errors or wrong camera position guesses affect the calibration results for each camera individually, and it is a tough task to calibrate all cameras with the same precision. Thus, we find that the critical result of our collaboration is to work on the compatibility of different software using the calibration models studied, in order to minimize the drawbacks of any of them. For example, in the presented PTV experiment, if the camera position and focal length of the cameras are not known, the experiment is difficult to calibrate using the multimedia model, but the system can still be calibrated using the Soloff model if only the 2D and 3D marker positions are known and a direct conversion of the Soloff calibration to the multimedia model is possible. Another helpful example is the use of the well-established checkerboard calibration in multiple views at different angles by OpenPTV or MyPTV, while the method used in proPTV is not able to calibrate this setup because it requires exactly known plane positions. A third example is the use of a dumbbell or wand calibration in cases where the calibration target cannot be inserted, where the Soloff model also fails to calibrate the system, but the other models do not. Thus, learning to combine the different advantages of different open source packages, possibly through a unified framework optimized from a software architecture point of view, could be a good future direction for the experimental fluid mechanics community.

Data availability statement

The data that support the findings of this study are openly available at the following URL/DOI: https://github.com/OpenPTV/proPTV_OpenPTV_MyPTV_comparison.

ORCID iDs

R Barta https://orcid.org/0000-0001-8882-5864
A Liberzon https://orcid.org/0000-0002-6882-4191
R Shnapp https://orcid.org/0000-0001-7495-8420

References

[1] Zhang Y J 2023 *Camera Calibration 3-D Computer Vision: Principles, Algorithms and Applications* (Springer) pp 37–65

[2] Malik N, Dracos T and Papantoniou D 1993 Particle tracking velocimetry in three-dimensional flows *Exp. Fluids* **15** 279–94

[3] Maas H, Gruen A and Papantoniou D 1993 Particle tracking velocimetry in three-dimensional flows *Exp. Fluids* **15** 133–46

[4] Schröder A and Schanz D 2023 3D lagrangian particle tracking in fluid mechanics *Ann. Rev. Fluid Mech.* **55** 511–40

[5] Elsinga G E, Scarano F, Wieneke B and van Oudheusden B W 2006 Tomographic particle image velocimetry *Exp. Fluids* **41** 933–47

[6] Colomina I and Molina P 2014 Unmanned aerial systems for photogrammetry and remote sensing: a review *ISPRS J. Photogramm. Remote Sens.* **92** 79–97

[7] Zhang S 2018 High-speed 3D shape measurement with structured light methods: a review *Opt. Lasers Eng.* **106** 119–31

[8] Hartley R I and Sturm P 1997 Triangulation *Comput. Vis. Image Underst.* **68** 146–57

[9] Maas H G 1993 Complexity analysis for the establishment of image correspondences of dense spatial target fields *Int. Arch. Photogramm. Remote Sens.* **29** 102–7

[10] Samper D, Santolaria J, Brosed F J, Majarena A C and Aguilar J J 2013 Analysis of Tsai calibration method using two- and three-dimensional calibration objects *Mach. Vis. Appl.* **24** 117–31

[11] Meller Y and Liberzon A 2016 Particle data management software for 3dparticle tracking velocimetry and related applications–the flowtracks package *J. Open Res. Softw.* **4** e23–e23

[12] Shnapp R, Shapira E, Peri D, Bohbot-Raviv Y, Fattal E and Liberzon A 2019 Extended 3D-PTV for direct measurements of Lagrangian statistics of canopy turbulence in a wind tunnel *Sci. Rep.* **9** 7405

[13] Sturm P 2021 *Pinhole Camera Model Computer Vision: A Reference Guide* (Springer) pp 983–6

[14] Ruiz A, Liberzon A and Bhattacharya S 2023 Lagrangian turbulence statistics using 3D-PTV: realistic virtual experiment assessment *Flow Meas. Instrum.* **89** 102310

[15] Soloff S M, Adrian R J and Liu Z C 1997 Distortion compensation for generalized stereoscopic particle image velocimetry *Meas. Sci. Technol.* **8** 1441

[16] Ott S and Mann J 2000 An experimental investigation of the relative diffusion of particle pairs in three-dimensional turbulent flow *J. Fluid Mech.* **422** 207–23

[17] Barta R, Bauer C, Herzog S, Schiepel D and Wagner C 2024 proPTV: a probability-based particle tracking velocimetry framework *J. Comput. Phys.* **514** 113212

[18] Björck Å 1990 *Handbook of Numerical Analysis* vol 1 pp 465–652

[19] Yu C and Peng Q 2006 Robust recognition of checkerboard pattern for camera calibration *Opt. Eng., Bellingham* **45** 093201–093201

[20] Lu Y and Payandeh S 2007 Dumbbell calibration for a multi-camera tracking system *2007 Canadian Conf. on Electrical and Computer Engineering* (IEEE) pp 1472–5

[21] Horstmann G M, Schiepel D and Wagner C 2018 Experimental study of the global flow-state transformation in a rectangular Rayleigh-Bénard sample *Int. J. Heat Mass Transfer* **126** 1333–46

[22] Pribanic T, Salvi J and Kosovic M 2008 Calibration of 3D kinematic systems using 2D calibration plate *ISBS-Conf. Proc. Archive*

[23] Barta R and Wagner C 2024 Large scale reorientation in cubic Rayleigh-Bénard convection using particle tracking velocimetry

[24] Wieneke B 2008 Volume self-calibration for 3D particle image velocimetry *Exp. Fluids* **45** 549–56

[25] Wieneke B 2013 Iterative reconstruction of volumetric particle distribution *Meas. Sci. Technol.* **24** 024008

[26] Jahn T, Schanz D, Gesemann S, Schröder A and Schröder A 2021 Advanced iterative particle reconstruction for Lagrangian particle tracking *Exp. Fluids* **62** 179

[27] Shnapp R 2022 MyPTV: a Python package for 3D particle tracking *J. Open Source Softw.* **7** 4398

[28] Caron E, Witz J F, Cuvier C, Beaurain A, Magnier V and El Bartali A 2023 PYCASO: python module for calibration of cameras by Soloff's method *SoftwareX* **23** 101440

[29] Bhattacharya S and Vlachos P P 2020 Volumetric particle tracking velocimetry (PTV) uncertainty quantification *Exp. Fluids* **61** 197

[30] Belden J 2013 Calibration of multi-camera systems with refractive interfaces *Exp. Fluids* **54** 1–18

[31] Paolillo G and Astarita T 2021 On the PIV/PTV uncertainty related to calibration of camera systems with refractive surfaces *Meas. Sci. Technol.* **32** 094006

[32] Michaelis D, Mychkovsky A, Wiswall J, Prevost R, Neal D and Wieneke B 2021 Calibration correction of arbitrary optical distortions by non-parametric 3D disparity field for planar and volumetric PIV/LPT *14th Int. Symp. on Particle Image Velocimetry* vol 1

[33] Duane C B 1971 Close-range camera calibration *Photogramm. Eng.* **37** 855–66

[34] Hoyer K, Holzner M, Lüthi B, Guala M, Liberzon A and Kinzelbach W 2005 3D scanning particle tracking velocimetry *Exp. Fluids* **39** 923–34

[35] Holzner M, Liberzon A, Nikitin N, Lüthi B , Kinzelbach W and Tsinober A 2008 A Lagrangian investigation of the small-scale features of turbulent entrainment through particle tracking and direct numerical simulation *J. Fluid Mech.* **598** 465–75

[36] Gülan U, Lüthi B, Holzner M, Liberzon A, Tsinober A and Kinzelbach W 2012 Experimental study of aortic flow in the ascending aorta via Particle Tracking Velocimetry *Exp. Fluids* **53** 1469–85

[37] Meller Y and Liberzon A 2015 Particle–fluid interaction forces as the source of acceleration PDF invariance in particle size *Int. J. Multiph. Flow* **76** 22–31

[38] Neamtu-Halic M M, Krug D, Haller G and Holzner M 2019 Lagrangian coherent structures and entrainment near the

turbulent/non-turbulent interface of a gravity current *J. Fluid Mech.* **877** 824–43

[39] Engelen L and De Mulder T 2020 Application of 3D-PTV to mass exchange in an open-channel flow past a lateral embayment *Meas. Sci. Technol.* **31** 054004

[40] Brizzolara S, Rosti M E, Olivieri S, Brandt L, Holzner M and Mazzino A 2021 Fiber Tracking Velocimetry for Two-Point Statistics of Turbulence *Phys. Rev.* X **11** 031060

[41] Mann J, Ott S and Andersen J S 1999 *Experimental Study of Relative, Turbulent Diffusion* (Risø National Laboratory)

[42] Virtanen P *et al* SciPy 10 Contributors 2020 SciPy 1.0: fundamental algorithms for scientific computing in Python *Nat. Methods* **17** 261–72

[43] Shnapp R, Brizzolara S, Neamtu-Halic M M, Gambino A and Holzner M 2023 Universal alignment in turbulent pair dispersion *Nat. Commun.* **14** 4195

[44] Shnapp R and Holzner M 2024 Bubble-induced convection and flow instability in liquid vessels *J. Fluid Mech.* **996** A2

[45] Herzog S, Schiepel D, Guido I, Barta R and Wagner C 2021 A probabilistic particle tracking framework for guided and brownian motion systems with high particle densities *S N Comput. Sci.* **2** 1–20